Title
Imaging of location and geometry for extended targets using the response matrix

Journal
Journal of Computational Physics, 199(1)

ISSN
0021-9991

Authors
Hou, Songming
Solna, Knut
Zhao, Hongkai

Publication Date
2004-09-01

Peer reviewed

Available online at www.sciencedirect.com
SCIENCE DIRECT®
Journal of Computational Physics xxx (2004) xxx–xxx
JOURNAL OF COMPUTATIONAL PHYSICS
www.elsevier.com/locate/jcp

Imaging of location and geometry for extended targets using the response matrix

Songming Hou *, Knut Solna, Hongkai Zhao

Department of Mathematics, UCI Irvine, 103 MSTB, Irvine, CA 92697-3875, USA

Received 12 January 2004; received in revised form 17 February 2004; accepted 17 February 2004

Abstract

In this paper, we study how to image both the location and the shape of extended targets using the response matrix obtained from inter-element response of an active array of transducers. In particular, the time reversal technique is used for efficient initial localization of the target and the level set method is used for shape reconstruction. We then show how to couple the location estimation and shape reconstruction in a complementary way to improve accuracy for range estimation. Resolution analysis for active arrays in remote sensing regime is also presented. We illustrate with numerical experiments which show that the method is capable of imaging objects with complicated shapes and that the method is robust with respect to noisy data.

Keywords: Time reversal; Response matrix; Imaging; Level set method

1. Introduction

Active arrays of transducers that can send out signals and record reflected and/or transmitted signals are used in many applications such as medical imaging, non-destructive testing, seismic imaging, and target detection/recognition for sonar or radar systems. Such an active array can be used to probe a medium by sending out waves to illuminate reflective targets. Information about the targets can be extracted from the reflected and/or transmitted signals. In particular, the response matrix of an active array can be formed by recording the inter-element response, i.e., the response received at one transducer corresponding to an impulse sent out from another transducer. The product of the response matrix and its adjoint corresponds to the time reversal operator. The operator and its eigenvalues and eigenvectors have been studied extensively. For point scatterers it can be shown that the eigenspace of the time reversal operator is spanned by the illumination vectors, which are the wavefields at the array corresponding to a point source at one of the scatterers [7,16,18,19]. If the point scatterers are well separated, then there is a one-to-one corre-

* Corresponding author.
E-mail addresses: mickey@math.uci.edu (S. Hou), ksolna@math.uci.edu (K. Solna), zhao@math.uci.edu (H. Zhao).

0021-9991/$ - see front matter © 2004 Published by Elsevier Inc.
doi:10.1016/j.jcp.2004.02.010

spondence between the eigenstates of the time reversal operator and the illumination vectors. These relations have been explored to focus a wavefield on selected targets using iterated time reversal, called D.O.R.T [16,18]. The iterated time reversal procedure corresponds to the power method for finding the leading eigenvalues and eigenvectors for the time reversal operator. This relation was used for the MUtiple SIgnal Classification (MUSIC) algorithm for imaging locations of a set of point scatterers in [7,10,12,17], where the singular value decomposition (SVD) of the response matrix was used to find the eigenstates. The locations of well-separated scatterers can be found by matching the illumination vector of a searching point in the imaging space to the eigenstates. In this process the Green's function for the medium is used to construct the illumination vector for an arbitrary search point. However, the Green's function is unknown in general and has to be approximated in practice. Statistical stable imaging function were designed in [1] for point targets in a weakly inhomogeneous medium. There, a homogeneous Green's function was used, but statistical stability was achieved by time averaging from different frequencies in a broadband signal. This averaging means that incoherent parts of the measurements that comes from small scale medium heterogeneities are suppressed, thus giving a stabilized signal. They moreover obtain enhanced estimation of the range, the distance to the target, by explicitly using arrival time information. Recently in [2], this approach was extended to an algorithm that images the reflectivity function based on Born approximation and time reversal. It is shown that if the homogeneous Green's function is used to approximate the real Green's function for imaging in a weakly random medium, then the imaged reflectivity field is the true reflectivity function convolved with a Gaussian kernel which depends on the statistical property of the medium.

However, most of the studies above are mainly focused on point scatterers and their locations. The geometry of extended targets, scatterers with finite size that is comparable with wavelength, is not involved. In many applications, such as target identification, geometry plays a crucial role. For extended targets, the eigenstates of response matrix and hence the time reversal operator becomes more complicated. For example, it was shown in [5] that compressibility contrast and density contrast can generate different wavefields and hence multiple eigenstates even for a small spherical scatterer. The analysis was also extended to an arbitrary scatterer of finite size in [4], whereas the number of significant eigenstates for a finite aperture array is analyzed in [23]. Our starting point is the approach taken in [24], where the leading eigenstates and eigenvalues of the time reversal operator are used to characterize both the location and the dimensions of an extended target in the remote sensing regime. The result presented shows that the dominant eigenstate in the extended scatterer case also corresponds to the location of the target. As a consequence the techniques used for imaging point scatterers can still be applied to localize extended targets. Here, we continue this line of work by designing an algorithm that image both the location and the shape of an extended target(s) using the response matrix in the remote sensing regime. If we cast the problem in the standard inverse problem framework, we need to construct a functional that depends on both the location and the shape of the extended target. The process of carrying out these tasks simultaneously becomes ill-conditioned in the sense that optimization in spatial location and shape space are very different objectives, the spatial dimension is at most three whereas the shape space has an infinite dimension. Moreover, the inter-element response measurement is approximately an oscillatory integral on the support of the target. Without a good estimate of the location the shape estimation can be completely wrong due to the incorrect phase. The main goal of this paper is to illustrate the complications due to this coupling and the importance of decoupling at the initial stage using a relative simple setup. An important aspect of our approach is therefore an explicit strategy for partly separating, and then combining, the two tasks. In this paper, only a single frequency is used for the imaging algorithm. In future reports we will study the efficient use of different frequencies especially when the medium is inhomogeneous.

In this paper, we first show that if the location is known, then the shape estimation can be done efficiently and robustly from the response matrix using the level set method. In particular, the level set method allows us to find targets with complicated geometry and topology easily. We also provide a resolution analysis for

our algorithm which is verified by our numerical simulations. To localize the target(s), we first develop a multi-resolution imaging algorithm using the singular value decomposition of the response matrix. However, in the remote sensing regime, the location estimate, especially the range information, may not be very accurate when array aperture is small and/or target geometry is complicated. Here, we show that shape estimation can be used to improve location estimation. The key observation is an interesting pattern for the residual error in the shape optimization at different ranges. The pattern of the residual error after certain optimization steps has a periodic structure in range that is caused by phase coherence/incoherence which is analyzed in Section 5. Numerical experiments show that this pattern is robust with respect to noisy data. Using this pattern combined with an a priori rough location estimate using time reversal techniques, we get an improved location estimate. The subsequent shape optimization at the more accurate location moreover produces an improved shape estimate. In the shape estimation we use an elliptical region with center and dimensions determined by the response matrix as initial guess for the shape of the target. The shape estimation is then formulated as an optimization problem. We use the level set formulation to evolve the shape. To save computational cost, we apply the local level set idea.

The outline of the paper is as follows. First, in Section 2 we describe the experimental set-up, next, in Section 3 we develop a simple multi-resolution imaging algorithm using the SVD of the response matrix to obtain an a priori location estimate. Then, we use the response matrix and the level set method to design an algorithm for shape estimation given the location information in Section 4. We analyze the residual error pattern for shape optimization at different ranges and use it to improve the location estimate in Section 5. In Section 6, we provide a resolution analysis and present finally a set of numerical examples in Section 7, which confirms that the combined approach is capable of identifying complicated shapes and it is robust with respect to noisy data.

2. Target and Measurements

The setup of an active array and a target is illustrated in Fig. 1. The active transducer array is shown to the left and the planar target whose location and shape we want to estimate is shown to the right. Define the inter-element response $P_{ij}(t)$ to be the reflected signal at jth transducer corresponding to an impulse sent out from ith transducer. For an array consisting of N transducers, the matrix $P(t) = [P_{ij}(t)]_{N\times N}$ is called the response matrix. If the medium is static we have $P_{ij}(t) = P_{ji}(t)$ due to spatial reciprocity. If we assume that the medium and the array response is linear, for an output signal $\vec{e}(t) = [e_1(t), e_2(t), \ldots, e_N(t)]^{\mathrm{T}}$, where $e_i(t)$ is the output signal at ith transducer and T means transpose, the reflected signal at the array is

$$\vec{r}(t) = [r_1(t), r_2(t), \ldots, r_N(t)]^{\mathrm{T}} = P(t) * \vec{e}(t).$$

Here, $*$ denotes convolution in time, therefore, in frequency domain:

$$\vec{r}(\omega) = P(\omega)\vec{e}(\omega),$$

where ω is the frequency and $P(\omega)$ is the Fourier transform of $P(t)$. In this paper, the measurements that we use to estimate the target location and shape is this response matrix P at a single frequency.

We denote by $G(\boldsymbol{\xi}, \boldsymbol{x})$ the Green's function of the medium for frequency ω, which represents the wavefield at $\boldsymbol{x}$ for a point source located at $\boldsymbol{\xi}$. Due to the spatial reciprocity, $G(\boldsymbol{x}, \boldsymbol{\xi}) = G(\boldsymbol{\xi}, \boldsymbol{x})$. Observe that we will consider the case with time harmonic measurements and suppress the dependence on ω. To simplify the analysis, we assume that each transducer of the active array can be viewed as a point source and the target is a perfect reflector with a normal reflectivity that is equal to unity. In this case the reflected field can be represented as an integral over the illuminated surface. Hence, the response matrix can be written as

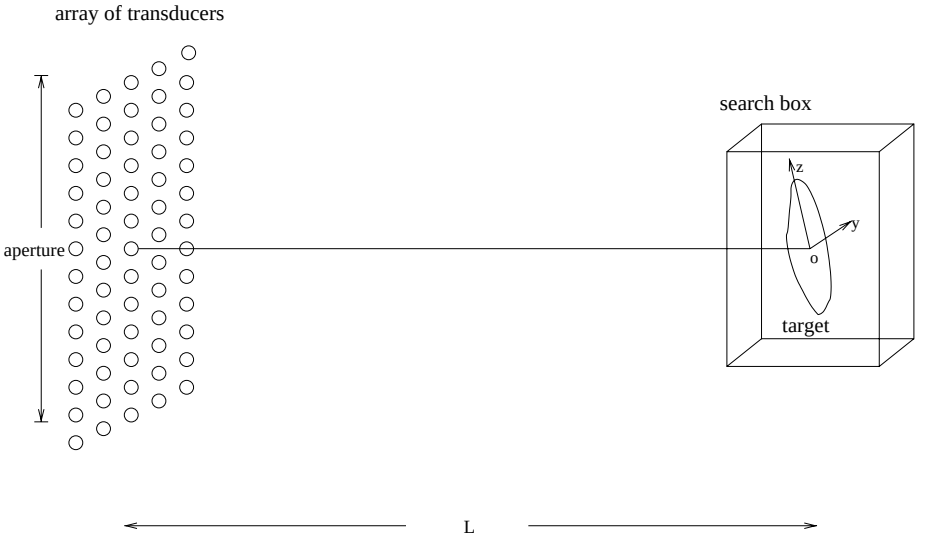

Fig. 1. The transducer of the active array is shown to the left in the plot. The target is at the range distance L.

$$P_{ij}(\omega) = \int_{\Omega} G(\boldsymbol{\xi}_i, \boldsymbol{x}) G(\boldsymbol{\xi}_j, \boldsymbol{x}) \tau(\boldsymbol{x}; \boldsymbol{\xi}_i, \boldsymbol{\xi}_j)\, \mathrm{d}\boldsymbol{x}, \tag{2.1}$$

where Ω is the part of the surface that can be illuminated by the active array and $\tau(\boldsymbol{x}; \boldsymbol{\xi}_i, \boldsymbol{\xi}_j)$ is a reflectivity kernel that depends on the incidence and outgoing angle, i.e., the angle between the normal of the surface at $\boldsymbol{x}$ and the vectors $\boldsymbol{\xi}_i - \boldsymbol{x}$ and $\boldsymbol{\xi}_j - \boldsymbol{x}$, respectively.

In remote sensing applications, such as target detections using sonar or radar system, the distance between the target and the active array is much larger than the wavelength and the size of the target and also the size of the array. In this case the wave from a transducer is almost planar when it reaches the target. Furthermore, we assume that from the point of view of the active array the target is planar which is parallel to the array surface. We are primarily interested in the remote sensing regime and we can therefore neglect the reflectivity kernel and approximate the response matrix by

$$P_{ij}(k) = \int_{\Omega} G(\boldsymbol{\xi}_i, \boldsymbol{x}) G(\boldsymbol{\xi}_j, \boldsymbol{x})\, \mathrm{d}\boldsymbol{x}, \tag{2.2}$$

which thus defines our modeling of the medium response.

3. A priori location estimate

The first step in our imaging procedure consists in finding an initial estimate for the location of the target. We use the response matrix, denoted by P as above, of an active array to image the target. We define the vector $\vec{g}(\boldsymbol{x}) = [G(\boldsymbol{\xi}_1, \boldsymbol{x}), \ldots, G(\boldsymbol{\xi}_N, \boldsymbol{x})]^{\mathrm{T}}$ to be the *illumination vector*. It is the wavefield at the array of transducers corresponding to a point source at a point $\boldsymbol{x}$. The first eigenvector $\vec{v}_1$ of P for an extended target is approximately aligned with the illumination vector of the center of target $\boldsymbol{x} = \boldsymbol{o}$ in the remote sensing regime [24]. We normalize $\vec{v}_1$ (as Matlab does) so that $\|\vec{v}_1\| = 1$. We construct the following imaging function as in [7]:

$$f(\boldsymbol{x}) = \frac{1}{\|\vec{g}(\boldsymbol{x})\|^2 - |\vec{g}(\boldsymbol{x})^{\mathrm{T}}\vec{v}_1|^2} = \frac{1}{\|[\vec{v}_1^{\mathrm{T}}\vec{g}(\boldsymbol{x})]\overline{\vec{v}_1} - \vec{g}(\boldsymbol{x})\|^2}, \tag{3.1}$$

where $\boldsymbol{x}$ is a search point and the bar means complex conjugate. The maximum of this imaging function gives a good lateral location estimate, but typically does not give satisfactory range estimate since the phase variation of the illumination vector across the array is not very sensitive to changes in the range especially in the remote sensing regime. The range estimate can be improved by using arrival time information and using more than one arrays. For weakly inhomogeneous medium, different imaging functions and their statistical stability were studied in [1].

In our numerical experiments, we use MATLAB to compute the singular value decomposition of the response matrix and get the leading eigenvector. Then, we construct the imaging function (3.1) using the homogeneous Green's function for $\vec{g}(\boldsymbol{x})$. We use two or three arrays and construct the imaging function as the product of these two or three ones. The maximum of the imaging function gives the a priori location estimate. A large offset in between the arrays improves the location estimate in all three spatial coordinates. The computation of the imaging function and searching for its maximum in a large region can be quite expensive. We briefly mention the idea of multi-resolution that was used to speed up the numerical searching process. First, in a large search box, we use a relatively coarse grid, which however is fine enough to capture the peak of the imaging function. Then one narrow the search box down to a neighborhood of the peak and repeat the process with a finer grid and so on.

4. Imaging target shape

In this section, we discuss the shape estimate of extended targets using the response matrix. Here, we assume that the distance in between the array and the target plane L is given, i.e., $\boldsymbol{x} = (L, y, z)$. We want to find a region Ω_t in the target plane that minimizes the following imaging functional:

$$F(\Omega) = \|P(\Omega) - P^{\mathrm{true}}\|_F^2 = \sum_{i,j=1}(P_{ij}(\Omega) - P_{ij}^{\mathrm{true}})^2, \tag{4.1}$$

where P^{true} is the measured response matrix and $P(\Omega)$ is defined as in (2.2). Ω_t is then taken as the shape estimate of the real target.

By calculating the shape derivative, i.e., the first variation of F in terms of a perturbation of $\partial\Omega$, the normal velocity at the boundary $\boldsymbol{x} \in \partial\Omega$ according to gradient descent is

$$v_{\mathrm{n}}(\boldsymbol{x}) = -\sum_{i,j=1}^{n}[(P_{ij}(\Omega) - P_{ij}^{\mathrm{true}})\overline{G(\boldsymbol{\xi}_i, \boldsymbol{x})G(\boldsymbol{\xi}_j, \boldsymbol{x})} + \overline{(P_{ij}(\Omega) - P_{ij}^{\mathrm{true}})}G(\boldsymbol{\xi}_i, \boldsymbol{x})G(\boldsymbol{\xi}_j, \boldsymbol{x})]. \tag{4.2}$$

We could also add a weighted length term for the boundary $\partial\Omega$ (area term in the case of a surface) as a regularization term if needed, i.e., minimize

$$F(\Omega) = \|P(\Omega) - P^{\mathrm{true}}\|_F^2 + \gamma|\partial\Omega|,$$

where γ is an appropriate choice of weight that may depend on the signal to noise ratio. Then, there will be a scaled curvature term in the normal velocity which will penalize against oscillations due to noise or numerical ill-posedness:

$$v_{\mathrm{n}}(\boldsymbol{x}) = -\sum_{i,j=1}^{n}[(P_{ij}(\Omega) - P_{ij}^{\mathrm{true}})\overline{G(\boldsymbol{\xi}_i, \boldsymbol{x})G(\boldsymbol{\xi}_j, \boldsymbol{x})} + \overline{(P_{ij}(\Omega) - P_{ij}^{\mathrm{true}})}G(\boldsymbol{\xi}_i, \boldsymbol{x})G(\boldsymbol{\xi}_j, \boldsymbol{x})] - \gamma\kappa,$$

where κ is the mean curvature. However, we find that our shape imaging technique works well without this regularization term and do not include it below.

Numerically we use the level set method to evolve an initial shape according to the above normal velocity to optimize the shape approximation. Recently, the level set method has been successfully used for shape evolution in optimal design and inverse problems [3,8,9,11,14,20]. The main advantage of the level set method is that one does not need to assume any a priori knowledge of the final shape. The level set method can deal with complicated geometry and topological changes easily. Let ϕ be the level set function whose zero level set represents the shape of the target, i.e.,

$$\Omega = \{\boldsymbol{x} \,|\, \phi(\boldsymbol{x}) < 0\}, \quad \partial\Omega = \{\boldsymbol{x} \,|\, \phi(\boldsymbol{x}) = 0\}.$$

The level set method turns the geometric problem of shape evolution into a time dependent partial differential equation:

$$\phi_t + v_n|\nabla\phi| = 0, \tag{4.3}$$

where t is just a pseudo-time in the optimization process and $\phi = 0$ at time t represents the shape at time t.

The numerical experiments we will present demonstrate that the optimization process is quite robust with respect to the initial guess. The normal velocity v_n at the boundary $\partial\Omega$ defined by (4.2) is extended to all $\boldsymbol{x}$, we can solve the level set Eq. (4.3) using well-developed numerical schemes for Hamilton–Jacobi equations [13,21]. However, the main issue here is the computational cost. The main cost in the optimization process is to compute v_n according to (4.2), which requires to compute each element of the response matrix $P_{ij}(\Omega)$ defined by the integral (2.2) for current shape Ω. This can be very costly if the array is large and we need to compute $v_n(\boldsymbol{x})$ at all $\boldsymbol{x}$. Here, we use the local level set method [15] so that we only calculate v_n within a narrow band near the zero level set and only update ϕ in the narrow band, see Fig. 2. Moreover, to evaluate the response matrix of the updated shape, we just need to form the response matrix of the symmetric difference between the old and updated shapes and then add that to the old response matrix. Here is the algorithm which we use to compute/update the response matrix for a shape given by the level set

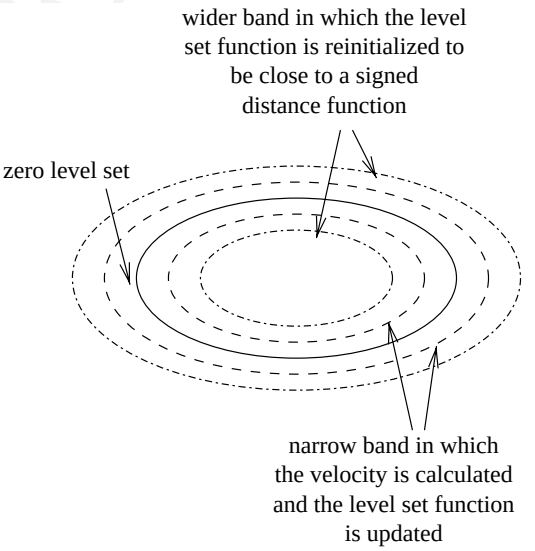

Fig. 2. The figure illustrates the local level set approach, only a band in the neighborhood of the boundary needs to be considered.

function ϕ. With a rectangular grid on the target plane, we classify all grid cells into three types: (1) interior cells: those cells whose four vertices have negative ϕ values; (2) exterior cells: those cells whose four vertices have positive ϕ values; (3) boundary cells: those cells whose four vertices have different signs of ϕ. The response matrix is the sum of contributions from the interior cells and the boundary cells. The contribution from an interior cell to $P_{ij}(\Omega)$ is simply the multiplication of the cell area with $G(\boldsymbol{\xi}_i, \boldsymbol{x})G(\boldsymbol{\xi}_j, \boldsymbol{x})$, where $\boldsymbol{x}$ is the center of the cell. To compute the contribution of a boundary cell, we construct a straight line approximation of the boundary $\partial\Omega$ and divide the cell into two regions, one that corresponds to $\phi < 0$, the other that corresponds to $\phi > 0$. The area and center of mass of the region corresponding to $\phi < 0$ can be easily calculated. The contribution from this boundary cell is the multiplication of the area of the region for $\phi < 0$ and $G(\boldsymbol{\xi}_i, \boldsymbol{x})G(\boldsymbol{\xi}_j, \boldsymbol{x})$, where $\boldsymbol{x}$ is the center of mass of the region for $\phi < 0$. Note that the response matrix of the whole region $\phi < 0$ is the sum of all these contributions. The response matrix of the symmetric difference mentioned above could be calculated cheaply by only considering those squares in which the area or center of mass of the region $\phi < 0$ changes when ϕ is updated. We next summarize this procedure.

4.1. Numerical algorithm

1. Initialize the level set function ϕ.
2. Compute the response matrix of the initial shape.
3. At each grid point in a narrow band near the zero level set, compute the normal velocity v_n according to (4.2).
4. Solve the level set PDE (4.3).
5. Reinitialize ϕ to be close to a signed distance function in a wider band.
6. Update the response matrix by comparing the old and new level set functions.
7. Go to step 3 until the required number of iterations is reached or the residue error is small enough.

Simple upwind ENO/WENO schemes are used for the level set Eq. (4.3). To speed up the optimization process while satisfying the CFL condition for stability, we choose the time step $\Delta t = \{C\}/\{\max_x v_n(\boldsymbol{x})\}$, where $0 < C < 1$ is a constant. For our numerical examples we take $C = 0.3$. For the reinitialization, we use the time marching scheme [22]

$$\phi_t + \mathrm{sign}(\phi_0)(|\nabla\phi| - 1) = 0,$$

where $\phi_0 = \phi(0)$, $\mathrm{sign}(\phi_0)$ is the sign function which is 1 if $\phi_0 > 0$, -1 if $\phi_0 < 0$, and 0 if $\phi_0 = 0$. More details about the finite difference schemes and the numerical sign function can be found in [15].

5. A posteriori location estimate

If the exact range L is used for the initial guess in the shape estimate, then the algorithm in the previous section is very robust and gives very good results in our test cases. If the initial cross range estimate is not very good, we need a large computational domain in the target plane and more time steps to move the initial shape to the correct location and find a good fit. Thus, the computational cost increases with a poor lateral location estimate, but we still get a good final shape estimate.

For a general approach, the critical issue is how to move and deform the trial shape to get a good approximation. In our setup, we can cast the problem in the following formulation: find the range L and the planar shape $\Omega \in R^2$ which minimizes

$$F(L, \Omega) = \|P(L, \Omega) - P^{\mathrm{true}}\|_F^2 = \sum_{i,j=1} (P_{ij}(L, \Omega) - P_{ij}^{\mathrm{true}})^2, \tag{5.1}$$

where Ω is in the plane that is parallel to the array and is of distance L from the array, i.e.,

$$P_{ij}(L,\Omega)=\int_{\Omega} G(\boldsymbol{\xi}_i,\boldsymbol{x})G(\boldsymbol{\xi}_j,\boldsymbol{x})\,\mathrm{d}\boldsymbol{x},\quad \boldsymbol{x}=(L,y,z).$$

Although shape estimate will reveal more detailed geometric information about the target, shape deformation is more expensive than localizing the target since the shape space is infinite. Moreover, without good range information shape optimization may be completely wrong due to the phase incoherence as will be shown below. That is why it is crucial to have a good range estimate with minimal shape dependence. Thus, we first use the time reversal technique to localize the target. After the location of the target is known approximately we need to couple the optimization in shape and location to get more accurate information. A straightforward way is to follow the gradient descent direction in both L and Ω for the energy functional (5.1). The shape derivative with respect to Ω is the same as in (4.2). The derivative in L is

$$\frac{\partial F(L,\Omega)}{\partial L}=2Re\left\{\sum_{i,j=1}^{n}\left[(P_{ij}(L,\Omega)-P_{ij}^{\mathrm{true}})\int_{\Omega}\frac{\partial G(\boldsymbol{\xi}_i,\boldsymbol{x})}{\partial L}G(\boldsymbol{\xi}_j,\boldsymbol{x})+G(\boldsymbol{\xi}_i,\boldsymbol{x})\frac{\partial G(\boldsymbol{\xi}_j,\boldsymbol{x})}{\partial L}\,\mathrm{d}\boldsymbol{x}\right]\right\}.$$

If we alternatively optimize in L and in Ω, i.e., every time step we optimize in L for a fixed trial shape Ω using the above formula and then update Ω with current L using the normal velocity (4.2), or vice versa, this optimization does not converge in general. Intuitively, one might expect similar robust behavior in the range direction as in the lateral direction. However, this is not the case. In the remote sensing regime, the distance between the target and the array is mainly determined by the range L. Hence, phase information at the transducer array is most sensitive to the change in L. Due to the periodic structure of phase coherence and incoherence in the range as explained below, there will be many local minimas. Moreover, we find a very robust pseudo-periodic structure for the residue error $E(L)=\min_{\Omega}\|P_{\mathrm{true}}-P(L,\Omega)\|_F^2$ in L. We show this pattern in Figs. 11–15. In our experiments, we only do a certain number of iterations for the optimization at each fixed L and plot the residue error in L. $E(L)$ has peaks and valleys and the pseudo-period is almost exactly half wavelength, $\lambda/2$, in our experiments. In each period, from one-fourth to three-fourths of the period, the residual is a constant, which is the largest residual in the period. If we plot the area of the optimized shape as a function of L instead, the same pseudo-periodic pattern is seen and the area is zero from one-fourth to three-fourths of each period, corresponding to the intervals with the largest residual.

Here, we give a simple explanation of this pattern.

Recall that the elements P_{ij} of the response matrix is the integral of the product of two Green's functions. The 3D homogeneous Green's function is

$$G(\boldsymbol{x},\boldsymbol{y})=\frac{\mathrm{e}^{\mathrm{i}k|\boldsymbol{x}-\boldsymbol{y}|}}{4\pi|\boldsymbol{x}-\boldsymbol{y}|}.$$

Assume L is the true range and is much larger than the aperture a, the size of the target and the center offset of the target. Denote $\hat{L}$ to be an approximate range. In this regime, we have:

$$|P_{ij}^{\mathrm{true}}-P_{ij}|\approx\left||\Omega_{\mathrm{true}}|\frac{\mathrm{e}^{2\mathrm{i}kL}}{(4\pi L)^2}-|\Omega|\frac{\mathrm{e}^{2\mathrm{i}k\hat{L}}}{(4\pi\hat{L})^2}\right|.$$

First, if $L-\hat{L}=n\lambda/2=n\pi/k$, where n is an integer, then by choosing $|\Omega|=|\Omega_{\mathrm{true}}|\hat{L}^2/L^2$, we have $|P_{ij}^{\mathrm{true}}-P_{ij}|\approx 0$. Thus, there are local minima of residuals with the spacing equals almost exactly $\lambda/2$, this is confirmed in Section 7. Moreover, the area of the shape corresponding to these local minima is a quadratic function in $\hat{L}$, which will also be confirmed in Section 7. Next, let $\theta=(4\pi/\lambda)(L-\hat{L})=2k(L-\hat{L})$. If $2n\pi<\theta<2n\pi+(\pi/2)$ or $2n\pi+(3\pi/2)<\theta<2n\pi+2\pi$, then for $|\Omega|=(\hat{L}^2/L^2)|\Omega_{\mathrm{true}}|\cos\theta>0$, we have

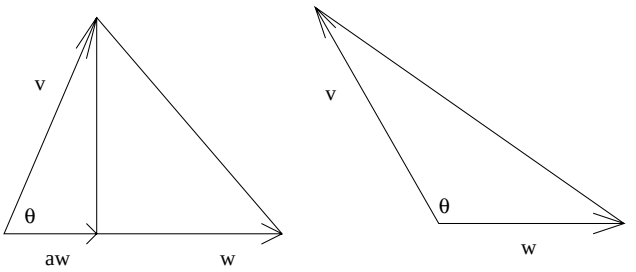

Fig. 3. Minimization of $\|\vec{v} - a\vec{w}\|$ with respect to non-negative a. When $\vec{v}$ and $\vec{w}$ form an acute angle (left figure), then the optimal a is positive, otherwise (right figure) the optimal $a = 0$.

$$\left| |\Omega_{\text{true}}| \frac{e^{2ikL}}{(4\pi L)^2} - |\Omega| \frac{e^{2ik\hat{L}}}{(4\pi\hat{L})^2} \right| = |\Omega_{\text{true}}| \frac{|\sin\theta|}{(4\pi L)^2} < \left| |\Omega_{\text{true}}| \frac{e^{2ikL}}{(4\pi L)^2} \right|.$$

This means that there is a non-vanishing "optimal shape" in this case. The left part of Fig. 3 shows the geometric explanation for the above algebraic calculation. Finally, assume that $2n\pi + (\pi/2) \leqslant \theta \leqslant 2n\pi + (3\pi/2)$, then there does not exist a positive $|\Omega|$ such that

$$\left| |\Omega_{\text{true}}| \frac{e^{2ikL}}{(4\pi L)^2} - |\Omega| \frac{e^{2ik\hat{L}}}{(4\pi\hat{L})^2} \right| < \left| |\Omega_{\text{true}}| \frac{e^{2ikL}}{(4\pi L)^2} \right|,$$

since obviously the left-hand side is the length of the side corresponding to an angle larger than or equal to $\pi/2$ in a triangle while the right-hand side is the length of another side of the same triangle, see the right part of Fig. 3. Thus, the the optimal shape at $\hat{L}$ is an empty set.

We can use this observation to improve the range estimation. The crucial point is that we do not really need precise shape information for this pattern. The shape we get at each $\hat{L}$ may be completely irrelevant. However, it is the shape optimization process and the residual error that will feed back into the range estimate and provide useful information. Assume an a priori range estimate $\hat{L}$ is obtained from the imaging function discussed in Section 3. Since the pseudo-period is $\lambda/2$, there will be a local minimum of the residual over $[\hat{L}, \hat{L} + (\lambda/2)]$. We can use a fine grid in the range direction for this one period, run a certain number of iterations for the shape optimization at each grid node and find this minimum L_1. Then, we carry out the shape estimation at depths $L_1 + (n\lambda/2)$ (with n an integer) and identify the depth with minimum residual. We expect it to be a very good estimate of the range with sub-wavelength accuracy, numerical experiments support this. The final shape estimate is the one associated with this a posteriori range estimate.

Although the pattern of the residue error is quite robust as is shown in our numerical experiments, when the shape is complicated or when there is noise, there is no way to guarantee that the global minimum occurs at the exact range L. To further improve the range estimate, we can use two or more frequencies to correlate more accurate range. For example, we can use two frequencies whose wavelengths are λ_1 and λ_2, respectively. Let $\hat{L}$ be the rough estimated range. Then, we use a fine grid to find the local minimums of residual using these two different frequencies in $[\hat{L}, \hat{L} + (\lambda_1/2)]$ and $[\hat{L}, \hat{L} + (\lambda_2/2)]$, respectively. We call them L_1 and L_2. Then, we minimize $|L_1 + m(\lambda_1/2) - L_2 - n(\lambda_2/2)|$ for integers m, n with small absolute value. The minimum should then occur when $L_1 + m\lambda_1 = L_2 + n\lambda_2 = L$. If the ratio λ_1/λ_2 cannot be represented using a fraction with both numerator and denominator small, this should give a unique minimum. We use numerical examples in Section 7 to illustrate this idea.

6. Resolution analysis

We discussed estimation of range L in the previous section and found that in the case with a homogeneous background we can obtain sub-wavelength accuracy by making use of the periodicity in the residue error. We illustrate this with numerical examples in the following section. Here, we discuss lateral resolution. According to Rayleigh's criteria in optics, the smallest distance between two far object that a telescope can resolve is given by $d = (1/1.22)(\lambda L/a)$, where the number 1.22 comes from the zero of a Bessel function. Analogously, we now study the smallest lateral distance between two objects that our array can resolve. To illustrate, we set up an experiment in which the targets are two circles with radius 0.5 m which are separated by 0.2 m. We use different λ, L, and a to test whether our algorithm can split the two target starting with an initial guess of a connected elliptical region. The results which we document in more detail in the following section show that $0.2m = d > C_1(\lambda L/a)$ is the essential criterion. In addition to this, there is another requirement in order to get the right shape: the spacing between transducers δa must not exceed certain constant C_2 times $\sqrt{\lambda L}$, otherwise the reflected wave is poorly sampled. Combining the two requirements above, we can adjust the parameters so that the true shape of target can be detected using the least number of transducers.

Now, we give a derivation for the above observations. We follow the notations in [2]. The time reversal point-spread function in homogeneous media is $\Gamma_0^{\mathrm{TR}}(y^s;t) = (1/2\pi)\int_{-\infty}^{\infty}\hat{\Gamma}_0^{\mathrm{TR}}(y^s;w)\mathrm{e}^{-\mathrm{i}wt}\,\mathrm{d}w$; where

$$\hat{\Gamma}_0^{\mathrm{TR}}(y^s;w) = \overline{\hat{f}(w)}\sum_{p=-N}^{N}\frac{\mathrm{e}^{\mathrm{i}k(|x_p-y^s|-|x_p-y|)}}{(4\pi)^2|x_p-y||x_p-y^s|},$$

where $x_p = ph/2$ and $h = a/N$ is two times the spacing δa between transducers, y is the source point and y^s is the search point.

In the remote sensing limit with ($a \ll L$), we can use the parabolic approximation

$$\mathrm{e}^{\mathrm{i}|x_p-y|} = \mathrm{e}^{\mathrm{i}k(L^2+x_p^2)^{1/2}} \approx \mathrm{e}^{\mathrm{i}k(L+(x_p^2/2L))}. \tag{6.1}$$

Similarly,

$$|x_p - y^s| = [L^2 + (\xi - x_p)^2]^{1/2} \approx L + \frac{(\xi - x_p)^2}{2L}.$$

Using this approximation, we have

$$\hat{\Gamma}_0^{\mathrm{TR}}(y^s;w) \approx \frac{\overline{\hat{f}(w)}}{(4\pi L)^2}\mathrm{e}^{\mathrm{i}k(\xi^2/2L)}\sum_{p=-N}^{N}\mathrm{e}^{-\mathrm{i}k(x_p\xi/L)}.$$

Since $x_p = ph/2$, we have the geometric sum

$$\sum_{p=-N}^{N}\mathrm{e}^{-\mathrm{i}k(x_p\xi/L)} = \frac{\exp\left\{\frac{\mathrm{i}kNh\xi}{2L}\right\} - \exp\left\{-\frac{\mathrm{i}k(N+1)h\xi}{2L}\right\}}{1-\mathrm{e}^{-(\mathrm{i}kh\xi/2L)}} = \frac{\sin\left(\frac{k(N+\frac{1}{2})h\xi}{2L}\right)}{\sin\left(\frac{kh\xi}{4L}\right)}.$$

Let

$$\frac{k(N+\frac{1}{2})h\xi}{2L} = \pi.$$

Then, $\xi \approx (\lambda L/a)$, since $a = Nh$ and $\lambda = 2\pi/k$.

This justifies our observation that the criteria to tell one target from the other is, the separation distance must be greater than a constant times $\lambda L/a$.

Furthermore, the period of the denominator must be much larger than the period of the numerator otherwise the peaks will be so close to each other that when convolved with two pulses, there is no separation in the result. This requires $N \geqslant 2$ approximately.

Assume next that we are not so deeply into the remote sensing regime. One must still resolve the phase variation in $\hat{I}_0^{\mathrm{TR}}$, moreover, the analysis assumes that we are in the parabolic regime with respect to the sampling interval δa. The parabolic approximation (6.1) requires essentially

$$\frac{kx_1^2}{2L} < C_2^2\pi,$$

for some constant C_2, which gives the sampling criterion $h < 2C_2\sqrt{\lambda L}$ or $\delta a < C_2\sqrt{\lambda L}$, where $\sqrt{\lambda L}$ is the Fresnel length. With this criterion, we obtain wavelength accuracy in the near field and the Rayleigh resolution in the remote sensing regime as illustrated in the following section.

7. Numerical experiments

In this section, we show numerical experiments to illustrate the performance of the imaging procedure described above. In Section 7.1, we calculate the a priori location estimate, which also gives us an initial guess. In Section 7.2, we use the exact range and almost no offset in transversal direction to assess the performance of the shape estimation procedure. As discussed above the level set method is used to minimize the residual and find the shape of the target(s). In Section 7.3, we provide experiments to show how the shape estimation algorithm can be used to help improving the location estimate and obtain sub-wavelength accuracy. Finally, in Section 7.4, we provide experiments to illustrate resolution issues.

7.1. A priori location estimate

We let the target be located in the (y,z)-plane. The exact range in our experiments is $500m$. The wavenumber used is 4π. To obtain the a priori location guess we use the search box $300m < x < 700m,\ -100m < y < 100m,\ -100m < z < 100m$. We use three groups of arrays of transducers to search for the location of the target(s). The centers of the arrays are at $(0,y_1,z_1)$, $(0,y_2,z_2)$, and $(0,y_3,z_3)$, where $y_1 = -y_2 = 100m,\ y_3 = 0,\ z_1 = z_2 = 0,\ z_3 = 170m$. The aperture of each group of the two-dimensional arrays is $a = 15m$.

In practice the response matrices are formed by physical experiments. In our numerical examples, we form them numerically by using the homogeneous Green's function and discretizing the integral in (2.2) over the target(s). We apply the multi-resolution procedure to search for the location of the target(s). First, we use a coarse grid $h_x = h_y = h_z = 4m$ to search for the approximated location of the target(s). The imaging function is the product of the three imaging functions (as in (3.1)) corresponding to the three response matrices of the three groups of arrays of transducers. For the target with a "happy face" shape (shown in Fig. 5), the sharp maximum occurs at $x = 512m,\ y = 0,\ z = -4m$.

Next, we use a fine grid $h_x = h_y = h_z = 0.2m$ in a small search box $(512-10)m < x < (512+10)m, -5m < y < 5m, (-4-5)m < z < (-4+5)m$, which is the neighborhood of the approximate center. The new maximum occurs at $x = 505.2m,\ y = 0,\ z = -2.2m$.

We observe similar behaviors for other configurations, too.

7.2. Shape estimate

In this section, we use the exact range L and minimize the functional (4.1) using the level set method for shape estimation described in Section 4. We want to see in the ideal situation how well the shape can be estimated and will discuss resolution issue and how to handle more general situations later.

We let $L = 500m,\ k = 20\pi$, and a grid size $h = 0.1m$ on the target plane. The square array consists of 5-by-5 transducers with a aperture $a = 50m$. The target has a shape with four leaves $r = 1 + 0.5\cos(4\theta)$. The initial guess is chosen to be a circle with the same center as the target. Fig. 4 shows the initial guess, the true solution and the numerical solution after 200 iterations. The result is very good, the complex geometry can be identified.

We keep the setup unchanged and let the target be a multiple connected region that looks like a happy face. This complicated shape can be represented cleanly as the max/min of several simple level set functions. We start with an elliptical initial guess, which is simply connected. Clearly topological changes have to happen during the iterations if the true shape could be found. We do observe topological changes and these are automatically taken care of due to the nice feature of the level set formulation. Fig. 5 shows the true solution and the very precise numerical approximation after 200 iterations.

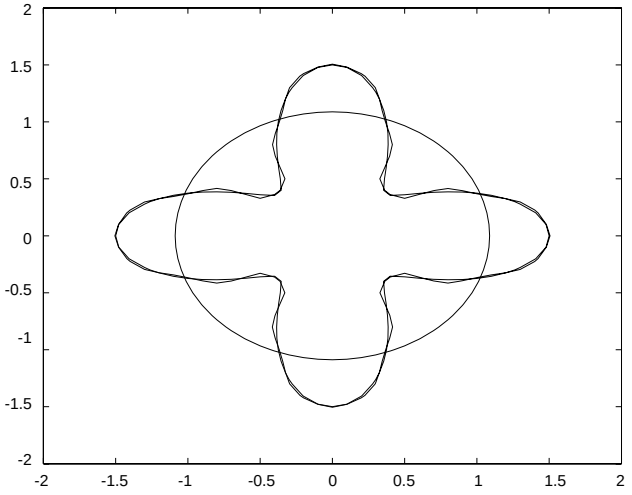

Fig. 4. Simply connected target with the shape of four leaves.

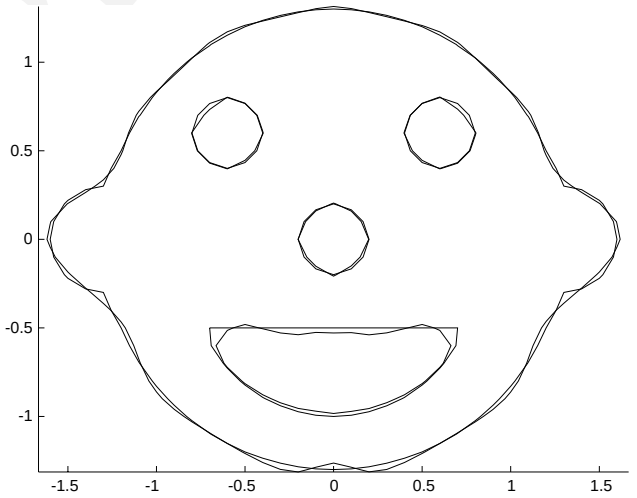

Fig. 5. Multiple connected target.

The holes are not generated away from the interface, since we used the local level set method which only changes the level set function near the interface. Instead, they are generated by a series of changes of curvature and concavity, as well as splitting and merging. The middle step(after 110 iterations) is shown in Fig. 6. Note that the curvature and concavity have changed from the initial guess(an ellipse) but the topology has not yet changed. During the next 90 iterations topological changes will happen, that is, merging and splitting will occur.

Next, we consider multiple targets. In our setup the multiple targets are in the same plane that is parallel to the array of transducers. Also the aperture of the array is small compared to the range. Hence, only those reflected/scattered waves that are traveling mainly along the range direction will be received by the array. That is why we neglect multiple scattering among the targets. We use three targets that resembles the letters "HOU". Again they can be represented by the max/min of simple level set functions. In order to capture the fine features we change our setup as follows: $L = 500m,\ a = 20m,\ k = 100\pi,\ h = 0.1m$. We use 6-by-6 transducer array. We increase the wavenumber to resolve the small gaps between the three letters, which is explained in the resolution analysis section. Again we use an elliptical initial guess and complicated topological changes occur to capture the true shape. Fig. 7 shows the true solution and the numerical solution after 250 iterations. The result is very good as our grid is relatively coarse with $h = 0.1m$, which barely resolve the true shape.

Now we consider the shape estimate using noisy data. For each element of the true response matrix, we add a random phase angle with uniform distribution in $[-0.14\pi, 0.14\pi]$. Then, we add a random magnitude multiple with uniform distribution in $[0.96, 1.04]$. Fig. 8 shows the true solution and the good numerical approximation after 200 iterations. The result is stable with respect to different realizations.

In the above experiments, we obtained good results in the ideal situation using the exact range L and an almost exact cross range estimate. Now we still use the exact range L but use a cross range estimate which is not perfect. The numerical result in the location estimate section gave a location error of $2.2m$ in the cross range. Now we use an elliptical initial guess with offset $2.2m$ and see if we could find the location and shape of the target.

Fig. 9 shows the initial guess with offset, the true solution and the numerical solution after 200 iterations. Since there is a shift, we use a larger calculation domain. The additional cost is not significant since we use

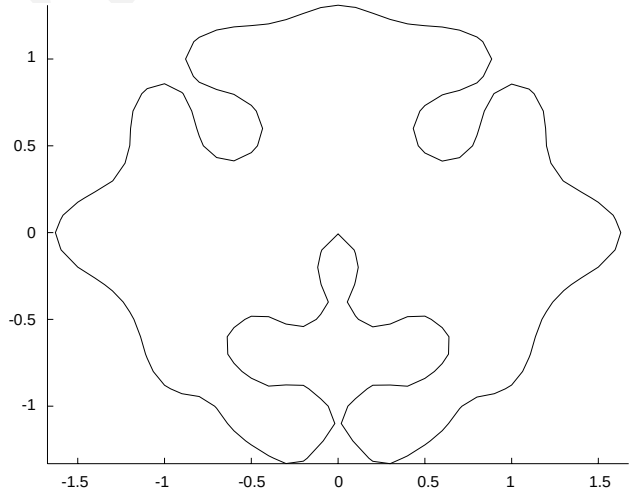

Fig. 6. Multiple connected target, middle step.

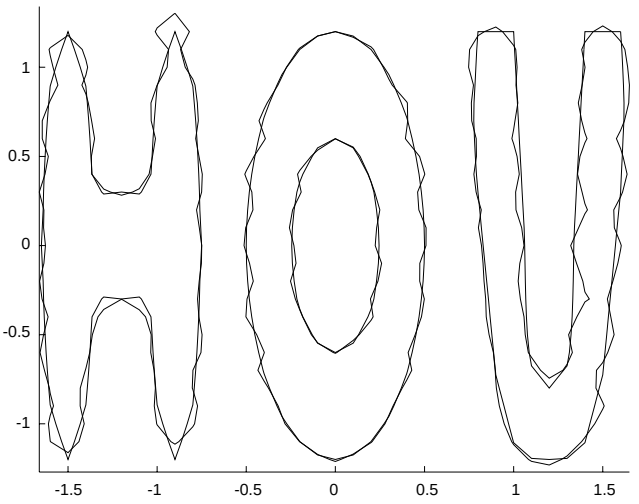

Fig. 7. Multiple targets with the shape of the letters "HOU".

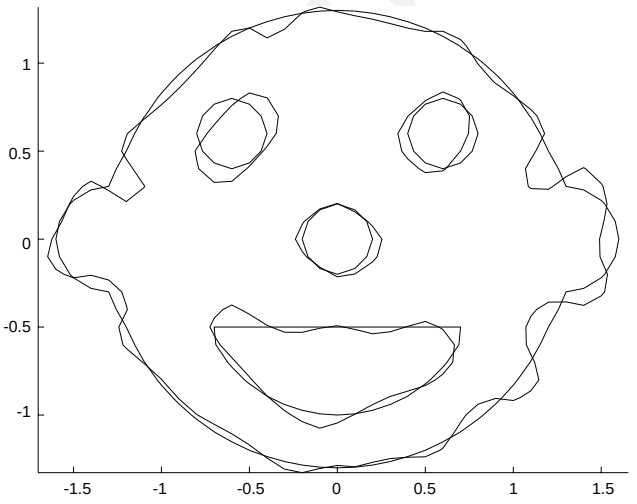

Fig. 8. Shape estimate using noisy data.

the local level set technique. As we can see from this figure, the result is good and the numerical approximation cannot be differentiated much from the curve for the exact solution.

With a larger shift, with no overlap between the initial guess and the true solution, such a good result can still be achieved, but the procedure requires more iterations in the optimization process for both moving and deforming the initial shape for a good fit. One way to accelerate the process is to apply the idea in [6] in which a set of small circles around the estimated center is used as the initial guess. If some of the circles fall into the position of the target, they will develop into the target and other small circles will vanish. Fig. 10 shows the result with 25 small circles as the initial guess. The radius of the small circles is as small as the grid size. This makes each early iteration very fast since we use the local level set technique and only compute the points near the boundary. After 700 iterations the numerical solution is almost identical with the true solution.

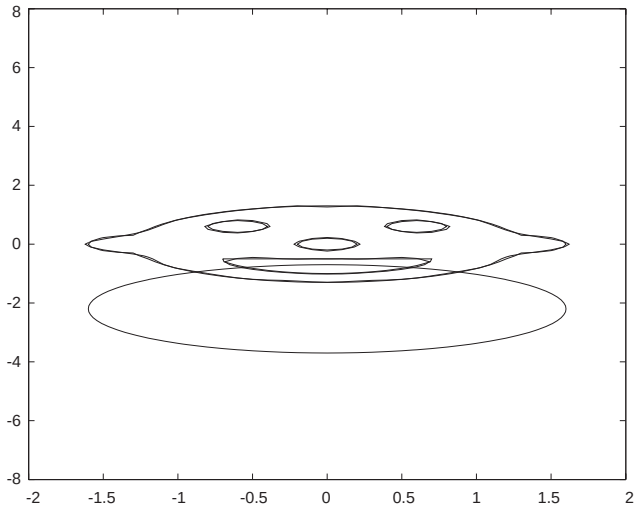

Fig. 9. Face shape target, a shifted ellipse as the initial guess.

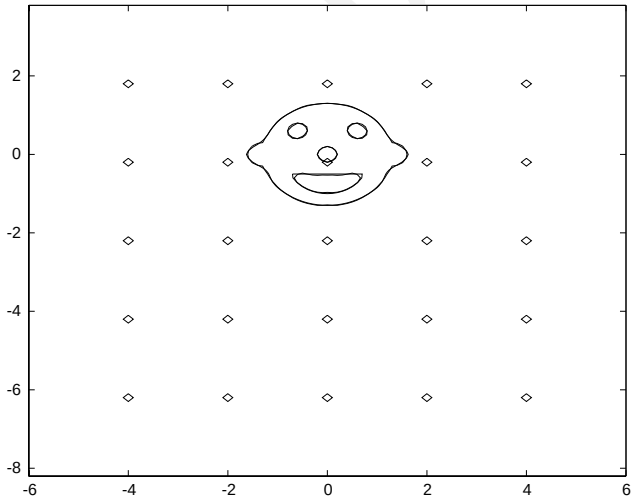

Fig. 10. Face shape target, 25 small circles as the initial guess.

7.3. Coupling the shape and location estimates

In this section we consider more general situations in which the range information is only approximately known. As we discussed in Section 5, the residual (as well as the area) after a certain number (100–200) iterations should have a pseudo-periodic pattern in the estimated range $\hat{L}$.

We use a circular target with radius $1m$. Let $L = 500m,\ a = 50m,\ \lambda = 5m,\ h = 0.1m$. 5-by-5 transducer array is used. The initial guess is a circle with radius $1m$ with no transversal offset but with a wrong range $\hat{L}$. Fig. 11 shows the base 10 log of the residual (after 200 iterations) as a function of $\hat{L}$. The pseudo-period is very close to $\lambda/2 = 2.5m$. Also in each period, the first $\lambda/8$ and the last $\lambda/8$ have values less than certain constant and in the middle $\lambda/4$ part, the value is a constant. This constant part corresponds to the zero area

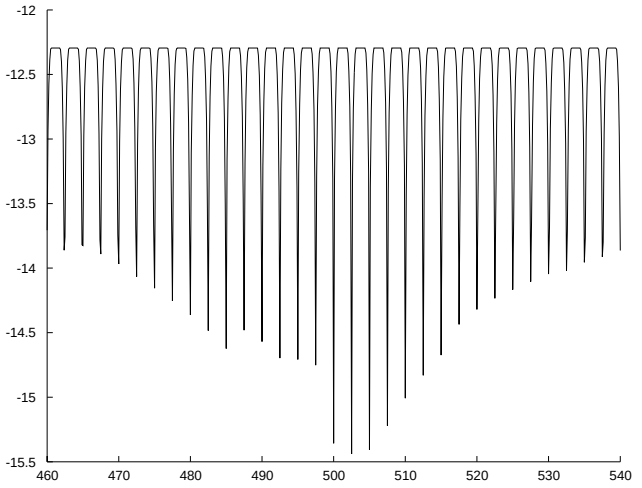

Fig. 11. Circular shape target, $\lambda = 5m$, log of residual as a function of $\hat{L}$.

433 approximation case and the constant is almost exactly log of the square of the F-norm of the true response
434 matrix. The global minimum occurs at $502.5m$. This is a good estimate for $L = 500m$. The error is at sub-
435 wavelength level.
436 We found above that the local maximums of the area should be approximately a quadratic function of $\hat{L}$.
437 Fig. 12 plots the area of the numerical shape (after 200 iterations) as a function of $\hat{L}$. We see the envelope
438 looks like a quadratic curve, as expected.
439 To further improve the location estimate, we use $\lambda = 0.5m$ instead. Fig. 13 shows the base 10 log of the
440 residual(after 200 iterations) as a function of $\hat{L}$. The pseudo-period is almost exactly $\lambda/2 = 0.25m$. Also in

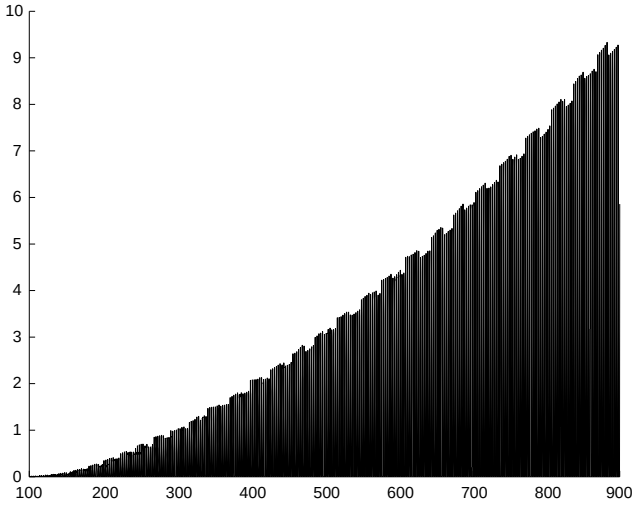

Fig. 12. Circular shape target, $\lambda = 5m$, area of the numerical shape as a function of $\hat{L}$.

each period, the first $\lambda/8$ and the last $\lambda/8$ have values less than certain constant and in the middle $\lambda/4$ part, the value is a constant as before. The global minimum occurs at $500m$. The error is very small in this case.

We comment that if we use the initial guess with an offset of about one or two meters in transversal direction, then the result is almost identical to what we have above.

Next, we use a more complicated target: the face. Let $L = 500m,\ a = 50m,\ \lambda = 0.1m,\ h = 0.1m$. 5-by-5 transducer array is used. The initial guess is an elliptical shape with almost exact transversal location estimate. Fig. 14 shows the base 10 log of the residual (after 300 iterations) as a function of $\hat{L}$. The pseudo-period is almost exactly $\lambda/2 = 0.05m$. Also in each period, the first $\lambda/8$ and the last $\lambda/8$ have values less than certain constant, and in the middle $\lambda/4$ part, the value is a constant. The global minimum occurs at $499.95m$. The error is $0.05m$.

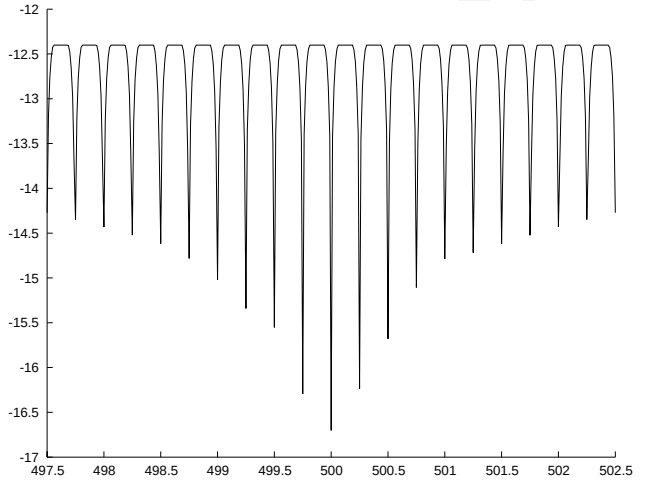

Fig. 13. Circular shape target, $\lambda = 0.5m$, log of residual as a function of $\hat{L}$.

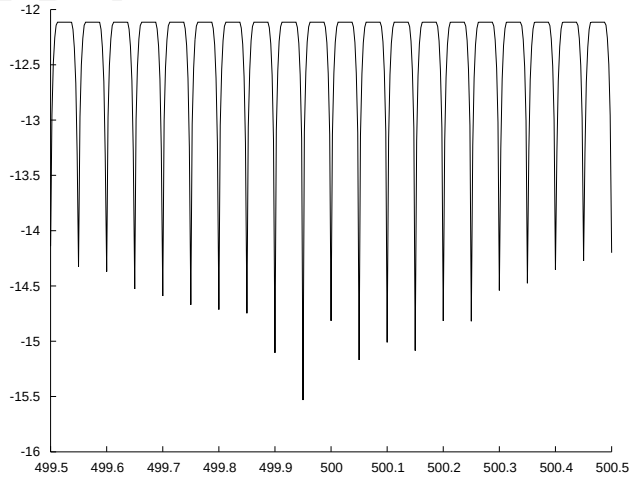

Fig. 14. Face shape target, $\lambda = 0.1m$, log of residual as a function of $\hat{L}$.

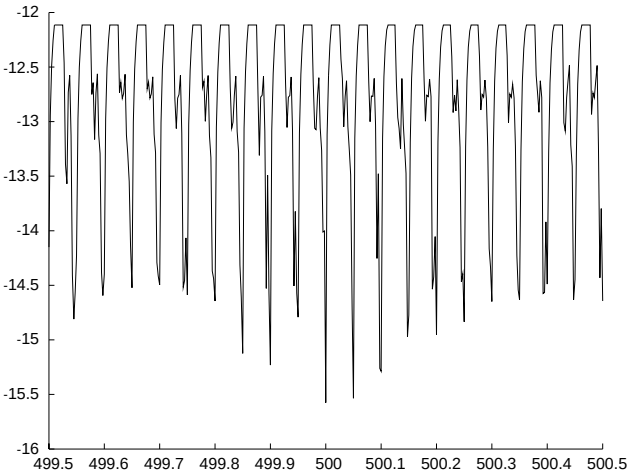

Fig. 15. Face shape target, shifted initial guess, $\lambda = 0.1m$, log of residual as a function of $\hat{L}$.

If we use the initial guess with an offset of about 1 or 2 m in transversal direction, the result is shown in Fig. 15. The pattern is not as clean as before. But the pseudo-period is still $\lambda/2 = 0.05m$. In each period we have similar behavior for the residual error. However, we no longer see the residual being a constant exactly in the middle half of each period. The reason is, our analysis in Section 5 assumes the existence of an optimal shape at each $\hat{L}$. But the numerical algorithm is not necessarily able to find the optimal shape. When we use a circle as the target, it is much easier to find the optimal shape. But when we use the face, a more complicated target, the optimal shape at $\hat{L}$ might not be found after hundreds of iterations. However, even in this case, we get the global minimum at $500m$ and the error is almost zero.

If the pattern above only holds when the data is exact, then it would be useless in practice. Next, we show that with noisy data, the pseudo-periodic pattern still remains.

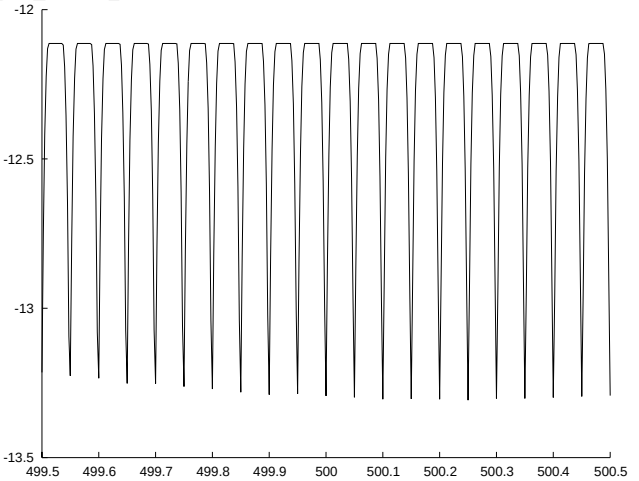

Fig. 16. Face shape target, noisy data, $\lambda = 0.1m$, log of residual as a function of $\hat{L}$.

For each element of the true response matrix, we add a random phase angle with uniform distribution in $[-0.14\pi, 0.14\pi]$. Then, we add a random magnitude multiple with uniform distribution in $[0.96, 1.04]$.

We use the same setup as above, with almost no transversal shift. Fig. 16 shows the base 10 log of the residual (after 300 iterations) as a function of $\hat{L}$. The pseudo-period is almost exactly $\lambda/2 = 0.05m$. Compared with the exact data case, the differences are, for noisy data the local minimums of residual are not as small as the exact data case. This is reasonable since for the noisy data, even with the exact range, we are unable to find a shape having the same response matrix as the data and hence the minimal residual is larger than the case with exact data. Also we no longer have the global minimum as a good estimate of the exact range. We will show that by using two different frequencies we could recover the range.

When the shape is more complicated or when there is noise, there is no way to guarantee that the global minimum occurs at the exact range L. Here, we illustrate how to correlate the locations of local minima of two different frequencies as explained in Section 5. For example, consider the face shape target. The rough range estimate is $\hat{L} = 505.2m$. By using $\lambda_1 = \pi$ and $\lambda_2 = 5$, we get the local minimums $L_1 = 506.29$ and $L_2 = 507.51$. Then, we minimize $|L_1 + m(\lambda_1/2) - L_2 - n(\lambda_2/2)|$ for integers m, n with absolute value less than 30. The minimum is 0.0031867, which occurs when $m = -4$ and $n = -3$. So $(L_1 + m\lambda_1 + L_2 + n\lambda_2)/2 = 500.008$ is our very accurate a posteriori range estimate. Note that in our choice the ratio $\lambda_1/\lambda_2 = \pi/5$. There is no rational number with denominator less than 35 that have value close to $\pi/5$ within 0.001. Therefore, there is no ambiguity when searching for the exact range L since the numerical errors are smaller than the magnitude of 0.001. Such a range estimate should be good enough to be used to find the shape of the targets.

7.4. Resolution analysis

We discussed resolution issue in Section 6. Here, we illustrate this with numerical examples to verify the qualitative results set forth there: The resolution is limited by the Rayleigh criterion value $\lambda L/a$, moreover, to achieve this resolution limit we need to obey the sampling criterion: $\delta a < C_2\sqrt{\lambda L}$.

To illustrate this, let the targets be two circles with radius $0.5m$ and separation distance $0.2m$. Let $L = 80m$, $\lambda = 1/3m$. We use only four transducers to image the target, that is, $\delta a = a$. Then, we need $\lambda L/C_1 d < a = \delta a < C_2\sqrt{\lambda L}$ in order to have a good shape estimate. So, we would expect that for very small

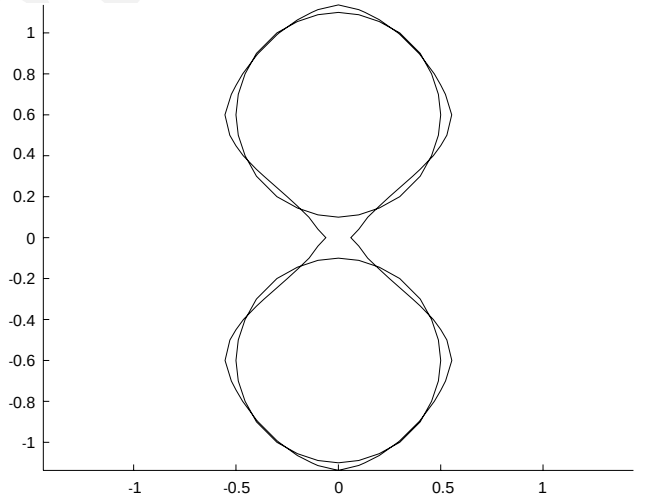

Fig. 17. Two circular targets, $a = \delta a = 10m$, a poor shape estimate due to violation of Rayleigh criterion.

488 a or very large a, we cannot get a good shape estimate and for a in middle range, we can obtain a satis-
489 factory shape estimate.
490 We let $a = 10m$, then from Fig. 17 we see that after many (hundreds of) iterations the shape we get is two
491 connected circles. The reason is, a is so small that the Rayleigh criterion inequality is violated.
492 Choose next $a = 40m$, then we get again very poor results as shown in Fig. 18. The reason is that $\delta a = a$
493 is so large that the sampling resolution criterion is violated.
494 Next, we let $a = 25m$. Then, we get a good estimate of the targets, the two criteria are satisfied and the
495 the two targets are well separated and resolved, see Fig. 19.
496 Now pick $a = 40m$ and $\delta a = 20m$, that is, we have nine transducers instead of four. With this finer
497 sampling for the large aperture, we get a very good estimate of the targets, see Fig. 20.

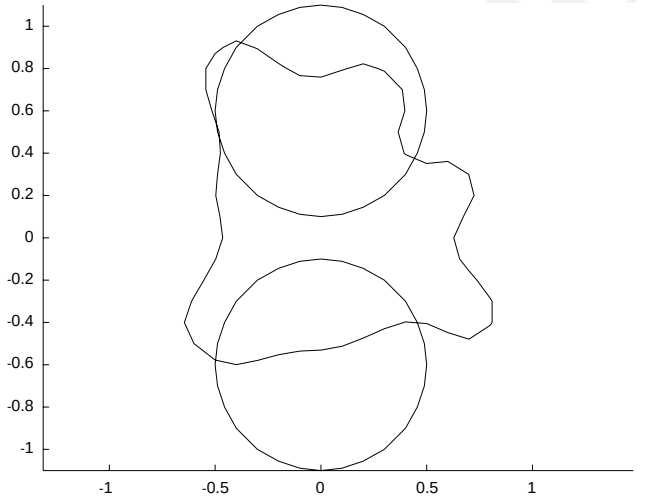

Fig. 18. Two circular targets, $a = \delta a = 40m$, a poor shape estimate due to violation of the sampling criterion.

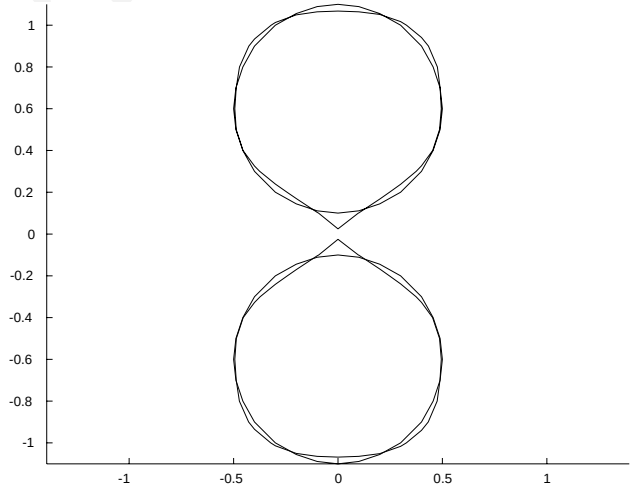

Fig. 19. Two circular targets, $a = \delta a = 25m$, we obtain a good estimate and resolve the two circles when both conditions are satisfied.

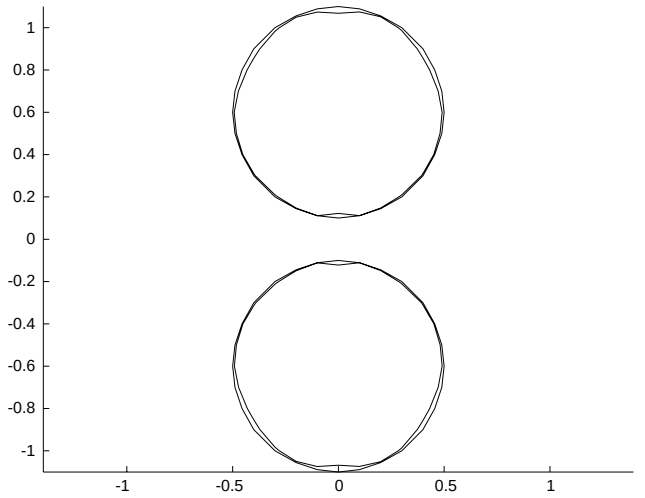

Fig. 20. Two circular targets, $a = 40m$, $\delta a = 20m$, more transducers allows for larger aperture and a very accurate shape estimate.

8. Conclusions

We present an imaging algorithm that can estimate both location and shape of extended targets. A key observation is that the optimization process is very ill-conditioned if these two estimates are coupled together at the initial stage. We use time reversal techniques to find a good estimate of the location. Then shape optimization is used to improve the location estimate. The crucial point in our formulation is that it is not the exact geometry information but the residual pattern in the shape estimate that provides us robust and useful information for location estimate. When more accurate location information is available, we use the level set method to find the shape. We use numerical experiments to show efficiency, accuracy, and robustness of our algorithms.

Acknowledgements

The research is partially supported by ONR Grant N00014-02-1-0090, DARPA Grant N00014-02-1-0603 and NSF Grant 0307011.

References

[1] J. Berryman, L. Borcea, G. Papanicolaou, C. Tsogka, Statistically stable ultrasonic imaging in random media, J. Acoust. Soc. Am. 112 (2003) 1509–1522.
[2] L. Borcea, G. Papanicolaou, C. Tsogka, Theory and applications of time reversal and interferometric imaging, 2003 (submitted).
[3] M. Burger, A level set method for inverse problems, Inverse Problems 17 (2001) 1327–1356.
[4] D.H. Chambers, Analysis of the time-reversal operator for scatterers of finite size, J. Acoust. Soc. Am. 112 (2) (2002) 411–419.
[5] D.H. Chambers, A.K. Gautesen, Time reversal for a single spherical scatter, J. Acoust. Soc. Am. 109 (6) (2001) 2614–2616.
[6] T.F. Chan, L.A. Vese, Active contours without edges, IEEE Trans. Image Process. 10 (2) (2001) 266–277.
[7] Devaney, Super-resolution processing of multi-static data using time-reversal and MUSIC, J. Acoust. Soc. Am. (2002), submitted.
[8] O. Dorn, E. Miller, C. Rappaport, A shape reconstruction method for electromagnetic tomography using adjoint fields and level sets, Electromagnetic Imaging and Inversion of the Earth's Subsurface, Inverse Problems 1 (2000) 1119–1156 (special issue).
[9] K. Ito, K. Kunish, Z. Li, The level-set function approach to an inverse interface problem, Inverse Problems 17 (2001) 1225–1242.

[10] E. Kerbrat, C. Prada, M. Fink, Imaging in the presence of grain noise using the decomposition of the time reversal operator, J. Acoust. Soc. Am. 113 (3) (2003) 1230–1240.
[11] A. Litman, D. Lesselier, F. Santosa, Reconstruction of a 2-d binary obstacle by controlled evolution of a level-set, Inverse Problems 14 (1998) 685–706.
[12] N. Mordant, C. Prada, M. Fink, Highly resolved detection and selective focusing in a waveguide using the d.o.r.t. method, J. Acoust. Soc. Am. 105 (5) (1999) 2634–2642.
[13] S. Osher, R. Fedkiw, Level set methods: an overview and some recent results, J. Comput. Phys. 169 (2001) 463–502.
[14] S. Osher, F. Santosa, Level set methods for optimization problems involving geometry and constraints I, J. Comput. Phys. 171 (2001) 272–288.
[15] D. Peng, B. Merriman, S. Osher, H. Zhao, M. Kang, A PDE-based fast local level set method, J. Comput. Phys. 155 (2) (1999) 410–438.
[16] C. Prada, S. Manneville, D. Spoliansky, M. Fink, Decomposition of the time reversal operator: detection and selective focusing on two scatterers, J. Acoust. Soc. Am. 99 (1996) 2067–2076.
[17] C. Prada, J.-L. Thomas, Experimental subwavelength localization of scatterers by decomposition of the time reversal operator interpreted as a covariance matrix, J. Acoust. Soc. Am. 114 (1) (2003) 235–243.
[18] C. Prada, J.-L. Thomas, M. Fink, The iterative time reversal process: analysis of the convergence, J. Acoust. Soc. Am. 97 (1) (1995) 62–71.
[19] C. Prada, F. Wu, M. Fink, The iterative time reversal mirror: a solution to self-focusing in the pulse echo mode, J. Acoust. Soc. Am. 90 (1991) 1119–1129.
[20] J. Sethian, A. Wiegmann, Structural boundary design via level set and immersed interface methods, J. Comput. Phys. 163 (2) (2000) 489–528.
[21] J.A. Sethian, Evolution, implementation, and application of level set and fast marching methods for advancing fronts, J. Comput. Phys. 169 (2001) 503.
[22] M. Sussman, P. Smereka, S. Osher, A level set approach for computing solutions to incompressible two-phase flows, J. Comput. Phys. 119 (1994) 146–159.
[23] M. Tanter, J.-L. Thomas, F. Coulouvrat, M. Fink, Acoustic time-reversal experiments in the nonlinear regime, J. Acoust. Soc. Am. 105 (2) (1999) 1232.
[24] H. Zhao, Analysis of the response matrix for an extended target, SIAM Appl. Math. (2003), to appear.